On the thermal and hydrothermal stability of spinel iron oxide nanoparticles as single and core-shell hard-soft phases

Marco Sanna Angotzi,[1,2,#,*] Valentina Mameli,[1,2,#] Dominika Zákutná,[3] Carla Cannas[1,2]

[1]*Department of Chemical and Geological Sciences, University of Cagliari, S.S. 554 Bivio per Sestu, 09042 Monserrato, Italy.*

[2]*Consorzio Interuniversitario Nazionale Per La Scienza e Tecnologia Dei Materiali (INSTM), Via Giuseppe Giusti 9, 50121 Florence, Italy*

[3]*Department of Inorganic Chemistry, Charles University, Hlavova 2030, 128 40, Prague 2, Czech Republic*

[#]*These authors contributed equally*

**Corresponding author: marcosanna@unica.it*

ABSTRACT

The thermal and hydrothermal stability of oleate-capped nanosized spinel iron oxides is of primary importance for the plethora of applications and environments for which they are employed. An *in-situ* XRD and *ex-situ* autoclave treatments have been set up for monitoring the thermal and hydrothermal stability in different samples. In detail, spinel iron oxide nanoparticles (NPs) were studied as (i) single-phase alone at three different sizes (about 6, 10, and 15 nm); (ii) as core in a core-shell architecture having cobalt ferrite as shell, at different core sizes (about 6 and 10 nm); (iii) as shell in a core-shell architecture with cobalt ferrite as core, at different shell thicknesses (about 3 and 4 nm). The Rietveld refinement of the diffraction patterns and ^{57}Fe Mössbauer spectroscopy have been exploited to monitor the evolution of the structural parameters and the hematite fraction. Moreover, transmission electron microscopy has permitted to deepen the morphological details on the phases. The spinel iron oxide-hematite transition has been found size- and time-dependent for the single-phase iron oxide NPs (360-455°C). The transition temperature has increased significantly when iron oxide is incorporated in a core-shell architecture, both as core (630 °C) and shell (520 °C), suggesting a stabilizing effect of cobalt ferrite. The hydrothermal stability of iron oxide and core-shell NPs has been found dependent on water content, time, and temperature, with a reducing effect of pentanol toward the formation of magnetite from maghemite, highlighted by ^{57}Fe Mössbauer spectroscopy. The synergic effects of cobalt ferrite and pentanol have limited the formation of hematite, leading to the obtainment of magnetite-covered cobalt ferrite NPs upon the hydrothermal treatment.

KEYWORD

Spinel iron oxide, hematite, core-shell, Mössbauer, X-ray diffraction, thermal-hydrothermal stability.

INTRODUCTION

Iron oxide nanoparticles (NPs) are some of the most studied and employed systems due to their non-toxicity, low cost, ease of manipulation, and unique chemical and physical (especially magnetic) properties.[1–3] Among the several applications of iron oxides, it is essential to cite catalysis,[4,5] biomedicine,[2,6,7] and environmental applications.[8–11] The most common and thermodynamically stable iron oxide phase is hematite (α-Fe_2O_3), featuring a hexagonal crystal structure (space group $R\bar{3}c$) and antiferromagnetic properties. Besides hematite, two other well-known metastable phases are magnetite (Fe_3O_4) and maghemite (γ-Fe_2O_3), having a spinel structure and ferrimagnetic properties. Spinels have a face-centred cubic (fcc) structure in which the oxygen atoms are cubic close-packed, generating tetrahedral (A)-sites and octahedral [B]-sites, occupied by trivalent and divalent cations. Magnetite contains both Fe^{II} and Fe^{III} in a 1:2 ratio, and its formula can be written as $(Fe^{III})[Fe^{II}Fe^{III}]O_4$. Maghemite comprises, as in magnetite, Fe^{III} in the tetrahedral and octahedral positions, but there are vacancies to compensate for the increased positive charge due to the oxidation of Fe^{II}. The cations are distributed randomly over the tetrahedral and octahedral sites, whereas the vacancies (which are also randomly distributed) are confined in the octahedral sites. The formula can also be written as $(Fe^{III})[Fe^{III}_{5/3}\square_{1/3}]O_4$, where □ represents vacancies. There can also be an intermediate compound where Fe^{II} persists: in this case, the formula would be $(Fe^{III})[Fe^{II}_{1-x}Fe^{III}_{1+2x/3}\square_{x/3}]O_4$, where x is 0 for pure magnetite and 1 for pure maghemite.[12]

For many applications that require magnetic features, magnetite or maghemite are desirable but, being metastable with respect to hematite, they are not always the primary component. In particular, it has been observed that spinel iron oxide can evolve to hematite due to high temperature (up to 500°C) and humidity (*e.g.*, aqueous colloidal dispersion), conditions that very often are present for some specific application.[13–17] Moreover, the transition in nanosized systems is size-dependent.[3,18–26] In the literature, there are several ways to stabilize the spinel iron oxides from phase transition. For instance, the organic coating can prevent contact among the NPs, avoiding sintering phenomena below the decomposition temperature.[27–29] Hydrophobic coatings can, moreover, distance water

molecules from the NPs surface, preventing oxidation.[27–30] The iron oxide phases can also be dispersed into an inorganic matrix, generating composites that separate the particles and block their growth.[25] Silica is, for example, a typical phase employed for stabilizing NPs from their phase transition, thanks to its high thermal stability and chemical inertia, in the form of porous or non-porous matrixes.[15,17,31–34] Indeed, it has been demonstrated that ultra-small spinel iron oxide NPs were formed inside the 2-3 nm pores of mesostructured silica (MCM-41) after calcination at 500 °C, then a phase transition into hematite has been observed after repeated cycles of sulfidation-regeneration at temperatures in the range 300-550 °C.[32] Besides the formation of composites, iron oxide can also generate a more intimate contact with specific inorganic phases that are able to grow epitaxially, forming heterostructures.[16,35–43] In principle, the formation of heterostructures with thermally stable phases should guarantee higher protection from the maghemite-hematite phase transition since the crystallographic planes are linked and locked with the other component.[44] Moreover, spinel ferrite-based heterostructures represent an exciting class of widely employed material thanks to the hard-soft magnetic coupling, for instance in the fields of magnetic heat induction and rare element-free permanent magnets.[38,43,45,46] Also, the morphology of the heterostructure certainly plays a crucial role in the stability of spinel iron oxide: dimers or multimers are expected to behave differently from, for example, core-shell NPs, where the iron oxide could also be the core or the shell.

In this context, an oleate-based solvothermal method has been set up to produce single-phase,[13,47–49] chemically mixed,[50,51] or heterostructured[16,42,43,52] spinel ferrite-based NPs with high crystallinity and low size dispersity. Moreover, iron oxide, in the form of magnetite/maghemite, has been engineered in a core-shell architecture as the shell with tunable thickness, coupled with manganese ferrite or cobalt ferrite. This latter phase is well-known to be chemically, mechanically, and thermally stable at high temperatures and represents an ideal candidate for protecting iron oxide toward phase transition.

For these reasons, this work focuses on the thermal and hydrothermal stability of the spinel iron oxide phase as in (i) single-phase NPs having various sizes, (ii) as core in iron oxide-cobalt ferrite core-shell heterostructures with different core diameter, and (iii) as shell in cobalt ferrite-iron oxide core-shell NPs featuring two shell thicknesses. Besides the characterization of the as-prepared samples by a multi-technique approach, the thermal stability was followed thanks to a powder X-ray diffractometer (XRD) equipped with a high-temperature chamber (HTC) by *in-situ* measurements in the temperature range 200-1300 °C and Rietveld refinement of the patterns. Instead, the hydrothermal stability was approached through solvothermal treatments in an autoclave by varying water content, solvent polarity, temperature, and time, and monitored through *ex-situ* XRD and ^{57}Fe Mössbauer spectroscopy.

1. EXPERIMENTAL

1.1 Chemicals

Oleic acid (>99.99%), 1-pentanol (99.89%), hexane (84.67%) and toluene (99.26%) were purchased from Lach-Ner; 1-octanol (>99.99%) and $Mn(NO_3)_2 \cdot 4H_2O$ (>97.0%) from Sigma-Aldrich; absolute ethanol and $Co(NO_3)_2 \cdot 6H_2O$ (99.0%) from Penta; NaOH (>98.0%) from Fluka; $Fe(NO_3)_3 \cdot 9H_2O$ (98.0%) from Lachema; $FeCl_2 \cdot 4H_2O$ (99%) from Merck.

1.2 Methods

Synthesis. Three different spinel iron oxide nanoparticles, labelled as FeA, FeB, and FeC, were prepared as described in previous works by solvothermal hydrolysis of metal oleates.[16,43,47,48,50] Two core-shell samples were prepared by covering FeA and FeB with cobalt ferrite (FeA@Co, FeB@Co). Two samples of cobalt ferrite (CoA, CoB) were covered with spinel iron oxide, obtaining CoA@Fe, CoB@Fe1, and CoB@Fe2. All core-shell samples were prepared through seed-mediated growth approach as described in previous work.[16,43] The synthesis conditions are summarized in Table 1S.

Thermal treatment. The thermal treatments were performed by high-temperature HTK 16N chamber (Anton Paar) at ambient condition through *in-situ* XRD experiments.

Hydrothermal treatment. The samples FeB, CoA@Fe, and CoB@Fe1 were subjected to further solvothermal treatment, described as follows. About 25 mg of nanoparticles were dispersed in 10 mL of toluene and put in a Teflon liner. Then, other organic solvents (pentanol, toluene) and, eventually, distilled water were added to the liner, which was insufflated with nitrogen and put vertically in a pre-heated oven (220 °C) for a certain time. After the treatment, the particles were separated by centrifugation and stored with 5 mL of hexane in a glass vial.

1.3 Characterization

The samples were characterized by X-ray diffraction (XRD), using a PANalytical X'Pert PRO with Cu K_α radiation (1.5418 Å), a secondary monochromator, Spinner sample chamber, and a PIXcel^{1D} position-sensitive detector. The samples were distributed on the glass sample holder and data were collected in the 5 – 90° of 2θ with the step size of 0.039°. For the *in-situ* high-temperature experiments, the powder samples were put on the Pt foil and the data acquisition was done with a step size of 0.039° from 22° to 38° of 2θ, to collect the most intense signals of spinel and hematite phases and minimize the time at each temperature step, from 200 °C up to 1100 °C depending on the sample under study.The peak position and instrumental width were calibrated using powder LaB_6 from NIST for both sample chambers. Refinement of the structural parameters[53] was performed by the Rietveld method using the MAUD software,[54] adopting the recommended fitting procedures.[55]

TEM images were obtained by using a JEOL 200CX operating at 160 kV. The particle size distribution was obtained by measuring over 1000 particles for each sample with the aid of the software Pebbles, setting a spherical shape for the elaboration.[56] The mean particle diameter was calculated as the average value and the dispersity as the percentage ratio between the standard deviation and the average value.

HRTEM images were carried out using JEOL JEM 2010 UHR equipped with a 794 slow-scan CCD camera.

Fourier Transform Infrared (FT-IR) spectra were recorded in the region from 400 to 4000 cm^{-1} by using a Bruker Equinox 55 spectrophotometer. Samples were measured in a KBr pellet. Spectra have been processed using OPUS software.

Thermogravimetric analyses (TGA) curves were obtained by using a PerkinElmer STA 6000, in the 25-850 °C range, with a heating rate of 10 °C min^{-1} under 40 mL min^{-1} O_2 flow.

Room temperature ^{57}Fe Mössbauer spectroscopy was performed on a Wissel spectrometer using transmission arrangement and proportional detector LND-45431. An α-Fe foil was used as a standard, and the fitting procedure was done by NORMOS program to determine the isomer shift (δ), quadrupole splitting (Q_s), hyperfine field (B_{hf}), and full width at half maximum of the signals.

2. RESULTS AND DISCUSSION

2.1 Thermal treatment of single-phase spinel iron oxide NPs.

Spinel iron oxide NPs with a narrow particle size distribution and having different sizes (FeA, FeB, FeC) were prepared through solvothermal hydrolysis of metal oleates (Table 1S).[16,43,48] The samples, characterized through XRD, TEM, HRTEM, and TGA (Figure 1, Figure 1S, 2S), show spinel structure, spherical shape, high crystallinity, cell parameter between the ones of bulk magnetite (8.396 Å, PDF#019-0629) and maghemite (8.3515 Å, PDF#039-1346), and mean particle size of 5.9(7) nm, 10.4(1.1) nm, and 14.8(1.5) nm for FeA, FeB, and FeC, respectively (Table 1).

Table 1. Lattice parameter (a), crystallite size (D_{XRD}), volumetric particle size (D_{TEM_V}), size distribution (σ), hematite starting and final temperature, theoretical iron oxide content, and experimental iron oxide content estimated from Rietveld refinement after the thermal treatment. Errors are reported in brackets.

Sample	a (Å)	D_{XRD} (nm)	D_{TEM_V} (nm)	σ (%)	Organic Content (%)	Starting temperature (°C)	Final temperature (°C)	Iron oxide th. (% w/w)	Iron oxide exp. (% w/w)
FeA	8.375(4)	5.8(1)	5.9	13	31	355	390	*n.a*	*n.a*
FeB	8.369(1)	11.8(1)	10.4	11	12.4	455	460	*n.a*	*n.a*
FeC	8.383(1)	17.5(1)	14.8	10	8.5	455	490	*n.a*	*n.a*
FeA@Co	8.400(1)	12.5(1)	14.5	14	11.2	*n.a*	*n.a.*	6	
FeB@Co	8.409(3)	17.1(1)	16.5	13	10.0	630	*n.a.*	23	19(5)
Co	8.399(8)	10.3(1)	7.5	14	19.5	*n.a*	*n.a.*	*n.a*	*n.a*
Co@Fe1	8.380(1)	14.3(1)	12.9	15	9.7	470	*n.a.*	79	84(9)
Co@Fe2	8.381(1)	17.0(1)	15.4	14	6.6	520	*n.a.*	87	76(6)

The samples were analyzed through room temperature (RT) ^{57}Fe Mössbauer spectroscopy (Figure 1) to deepen the structural and magnetic properties (Table 2S). The samples FeA and FeB reveal the presence of a singlet, indicating NPs in the superparamagnetic state, where the relaxation time of the superspins ($\tau_N = 10^{-9}$ s) is faster than the time resolution of the technique ($\tau_m \approx 10^{-7}$ s). Moreover, the singlet of FeB is wider than that of FeA, in accordance with the larger NP size and higher blocking temperature.[48] In contrast, the sample FeC features two overlapped sextets, corresponding to iron ions in octahedral (0.59(2) mm/s) and tetrahedral (0.45(1) mm/s) sites of magnetically blocked NPs. The values of isomer shift are particularly high for FeC indicating the presence of Fe^{II} and the formation of magnetite, or not-fully oxidized maghemite.

By looking at the thermogravimetric analyses (Figure 1C, Figure 1S), it is possible to observe the weight loss of oleate molecules in the range of 200-350 °C. Therefore, at temperatures below 350 °C, the iron oxide NPs are separated by the organic coating, preventing aggregation and sintering.

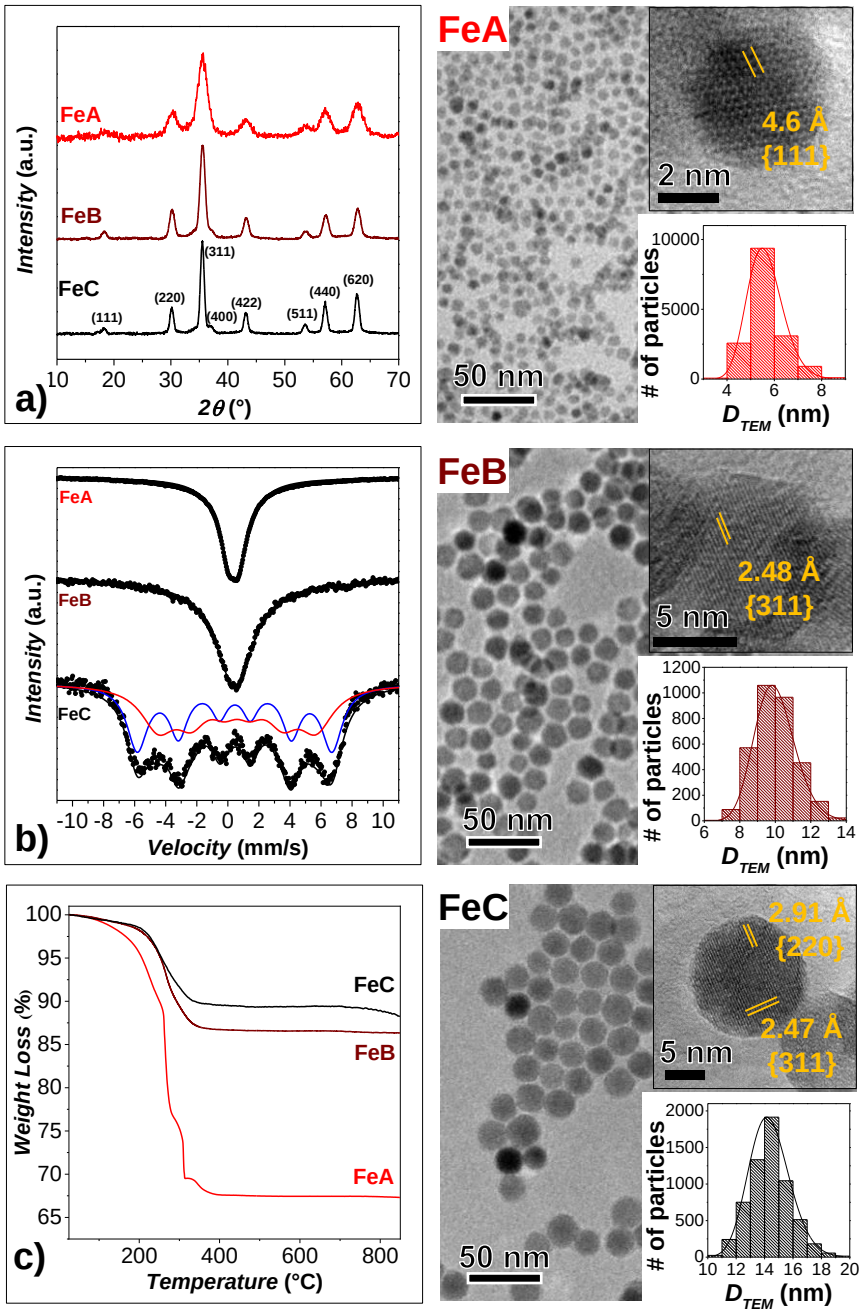

Figure 1. XRD patterns (a), ^{57}Fe Mössbauer spectra (b), TGA curves (c), TEM (right) and HRTEM (inset) micrographs with particle size distributions (inset) of the samples FeA, FeB, and FeC.

The iron oxide samples were thermally treated in an *in-situ* XRD chamber under air, to verify the spinel iron oxide-hematite transition temperature (Figure 2).

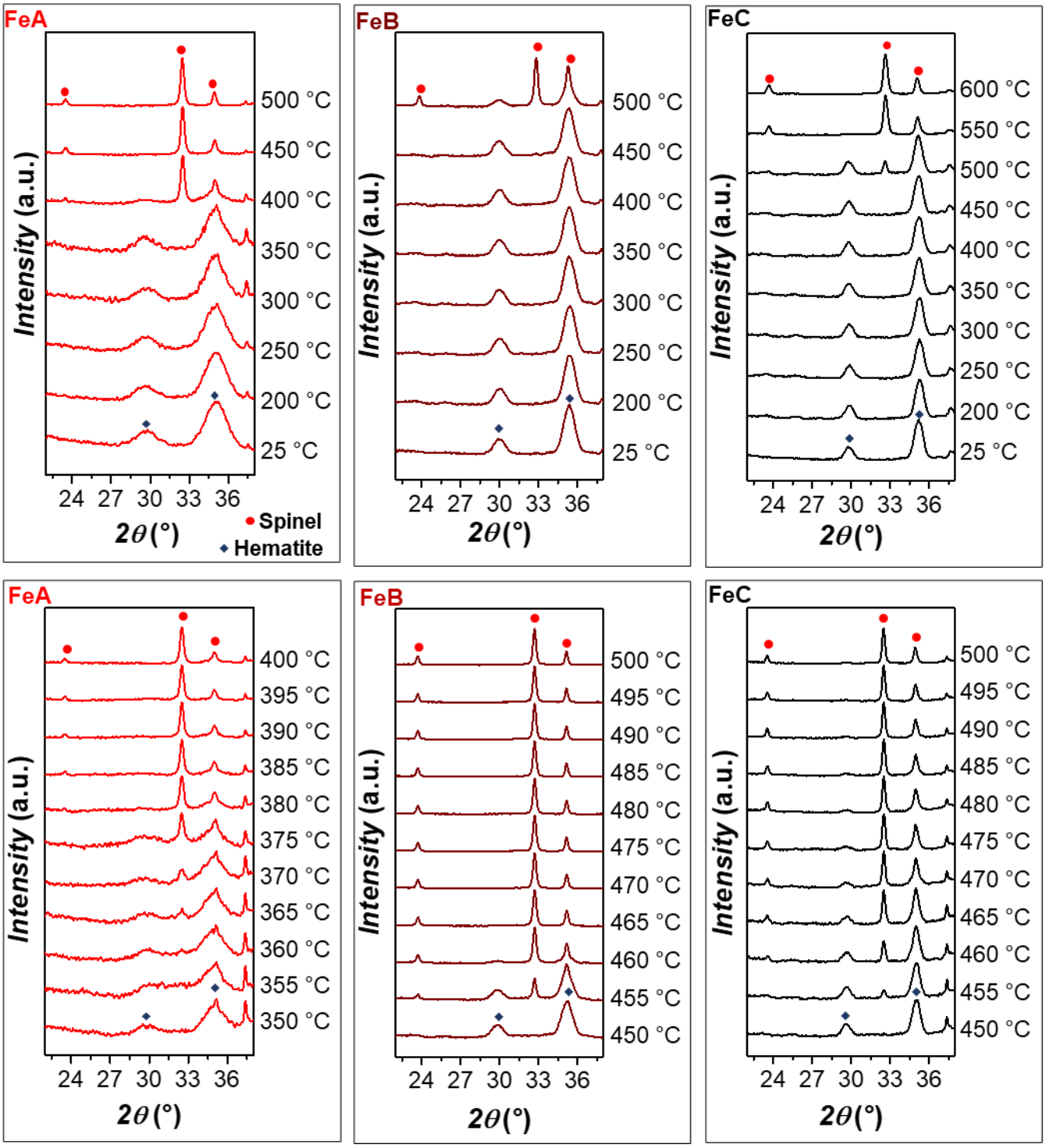

Figure 2. XRD patterns of the samples FeA, FeB, and FeC measured at different temperatures by *in-situ* XRD-HTC.

The samples were heated from 200 °C with a step of 50 °C up to the complete disappearance of the spinel phase. The hematite diffraction maxima (≈ 24° and 33°) appear for the first time at the temperature of 400 °C for FeA and 500 °C for FeB and FeC. Therefore, for a deeper investigation on the structural phase transition, a new portion of the samples were heated near the transition

temperature, with a step of 5 °C. The Rietveld refinements were done on the patterns before and after the appearance of the hematite peaks. Four approaches were initially attempted, fixing or refining the following parameters: overall isotropic displacement (B), microstrain (ε), and 2-theta offset (Ω) (Figure 3S-15S). Among these approaches, the ones that provided clear trends of the parameters were selected. For the evaluation of the lattice parameters (results labelled F), the best approach to refine the data was obtained fixing all B, ε, and Ω. In case to access the coherent domain size and the relative phase fraction, the only refined parameter was Ω (results labelled Ω). From the obtained results, it is visible, for FeA, a rapid rise of hematite fraction in the range 355-380 °C (Table 3S, Figure 4S, 5S).[28] The appearance of hematite is accompanied by an increase of the size of both the phases and the cell parameters *a* in the same temperature range, while the cell parameter *c* of hematite reduces. The spinel phase was detected till 390°C, featuring a crystallite size of about 8(1) nm. The coherent domain size of hematite instead stabilizes in the range 50-60 nm starting from 385 °C, as well as the cell parameters (a = 5.079(2) Å; c = 13.897(3) Å). The crystallite size agrees with the particle size observed in the TEM micrograph of the sample treated at 450 °C (Figure 16S).

The same experiments and evaluation approaches were conducted for the larger samples FeB and FeC, having NPs' sizes of 10.4(1.1) nm and 14.8(1.5) nm, respectively (Tables 4S, 5S, and Figures 6S-9S). Both FeB and FeC reveal a sudden transition temperature between 455-465 °C, one hundred degrees higher than FeA, caused by the larger particle size. For FeC, the hematite stops rising at about 490 °C, approximatively 30 °C higher than FeB. Observed higher transition temperature in FeC is caused by the larger particle size and the more considerable Fe^{II} amount content compared with the other samples leading first to the oxidation to maghemite followed by the conversion into hematite. For all samples, the coherent domain size of the hematite structure slowly increases with the temperature reaching the size of 60 nm at about 500 °C (400 °C for FeA). For FeC, above 500 °C up to 550 °C the hematite crystallite size reaches instead about 100 nm. For all samples (FeA, FeB, and FeC) the spinel crystallite size does not change much, except when its content is below 10 % w/w

and therefore affected by large errors. The trend of hematite cell parameters observed in the FeA was confirmed by the behaviour of FeC, showing the first increase of *a* or decrease of *c*, then a steady behaviour. On the contrary, for FeB, only the *plateau* region was visible, justified by the small maghemite-hematite transition range. The spinel cell parameter shows an increase due to thermal expansion for all samples but FeB, where the transition is short and the cell parameter is steady.

It is important to note that at temperatures below 350 °C, the iron oxide NPs are separated by the organic coating, preventing aggregation and sintering. As soon as the molecules decompose, the particle can get in touch, sinter, and generate large hematite crystals. For the smaller particles (FeA), this phenomenon is favoured at lower temperatures due to the closer packing and lower voids among the particles if compared to FeB and FeC. This result agrees with the findings from other authors for uncoated maghemite NPs, observing a transition temperature below 350 °C for 4 nm NPs,[24] and between 300 and 400 °C for NPs in the size range 6-10 nm.[26] In the case of capped NPs, the transition temperature depends also on the decomposition temperature of the coating molecules, as observed in our work. Indeed, for 4 nm caprylate-coated maghemite NPs, the transition occurred between 320 and 400°C, while in the case of poly(methyl methacrylate), higher temperatures were needed (400-500°).[28] Regarding the larger particles, transition temperatures above 450°C were observed also in the literature for uncoated maghemite NPs of about 12 nm.[57]

In the DTA curves (Figure 1S, bottom), a further endothermic peak is visible at 450 °C for FeA and 530 °C for FeB and FeC, corresponding to the hematite transition. The temperature is shifted about a hundred degrees higher than those observed for the diffraction analysis, because of the different heating steps of the two techniques. Indeed, a different temperature was also noted by changing the heating step of the *in-situ* XRD, indicating that the phase transition is also time-dependent, with first-order kinetics.[20,58] To support this observation, the FeB sample was treated to 455 °C, and XRD patterns were acquired at different times, as depicted in Figure 3a. Even though no hematite peaks are present at the beginning, they start rising after 10 minutes, confirming the time-dependence of the

phase transition. This is also encouraged by the morphology change observed from TEM micrographs, where micrographs taken after 9 minutes display aggregates of 10 nm spherical maghemite NPs (Figure 3b), while after the 10 min these aggregates generate sub-micrometric faceted hematite crystals, as clearly visible in Figure 3c.

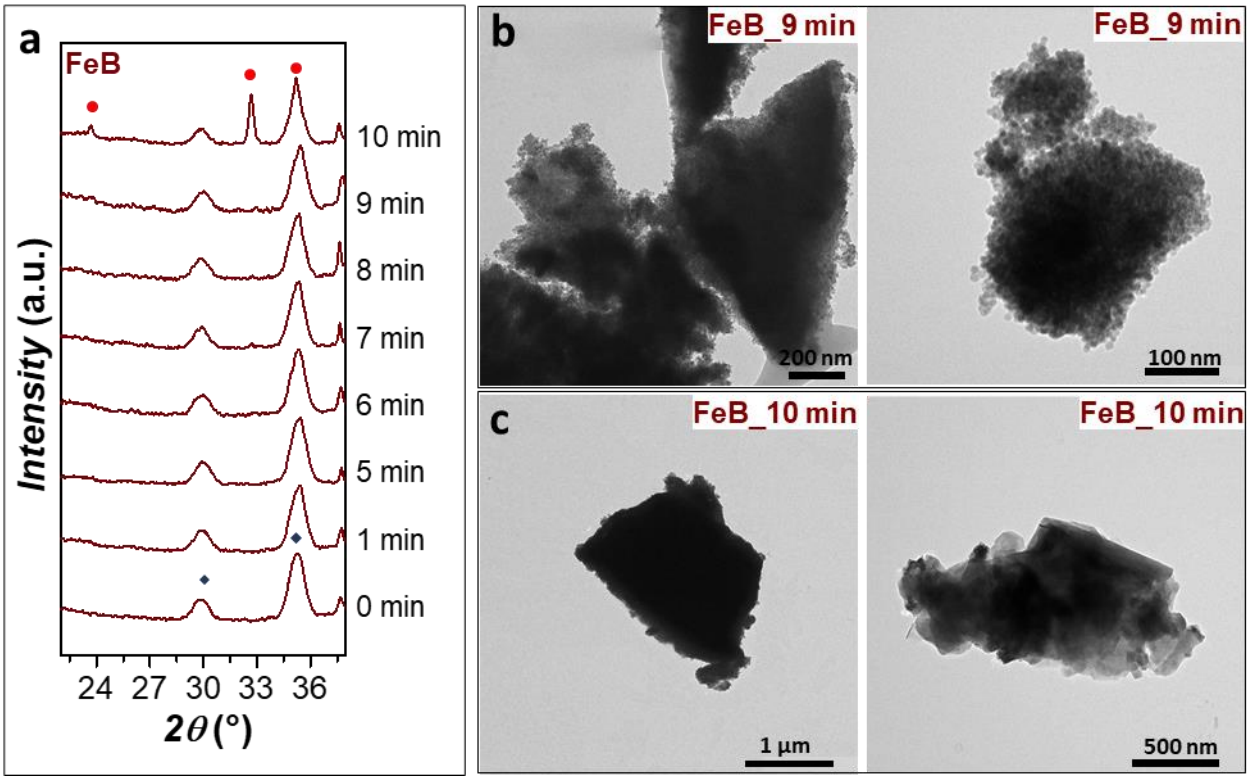

Figure 3. XRD patterns of the sample FeB measured at 455 °C and at different times by *in-situ* XRD-HTC (left) and corresponding TEM micrographs.

2.2 Thermal treatment of spinel ferrite-based core-shell NPs.

The thermal stability of iron oxide in NPs was also tested when iron oxide is in a core-shell architecture, either as core or shell. In recent works, we showed, through nanoscale chemical mapping (STEM-EELS and STEM-EDX), how it is possible to obtain spinel ferrite-based core-shell NPs with different core sizes, shell thicknesses, and the chemical nature of the shell.[16,42,43] Herein, two core-shell NPs were synthesized, starting from iron oxide having different sizes (FeA and FeB) and covering them with a shell of cobalt ferrite because of the high thermal stability of this latter phase

(FeA@Co, FeB@Co). Moreover, a sample of cobalt ferrite having a particle size of 7.5 nm was covered with spinel iron oxide having different shell thicknesses (Co@Fe1, Co@Fe2, Figure 4).

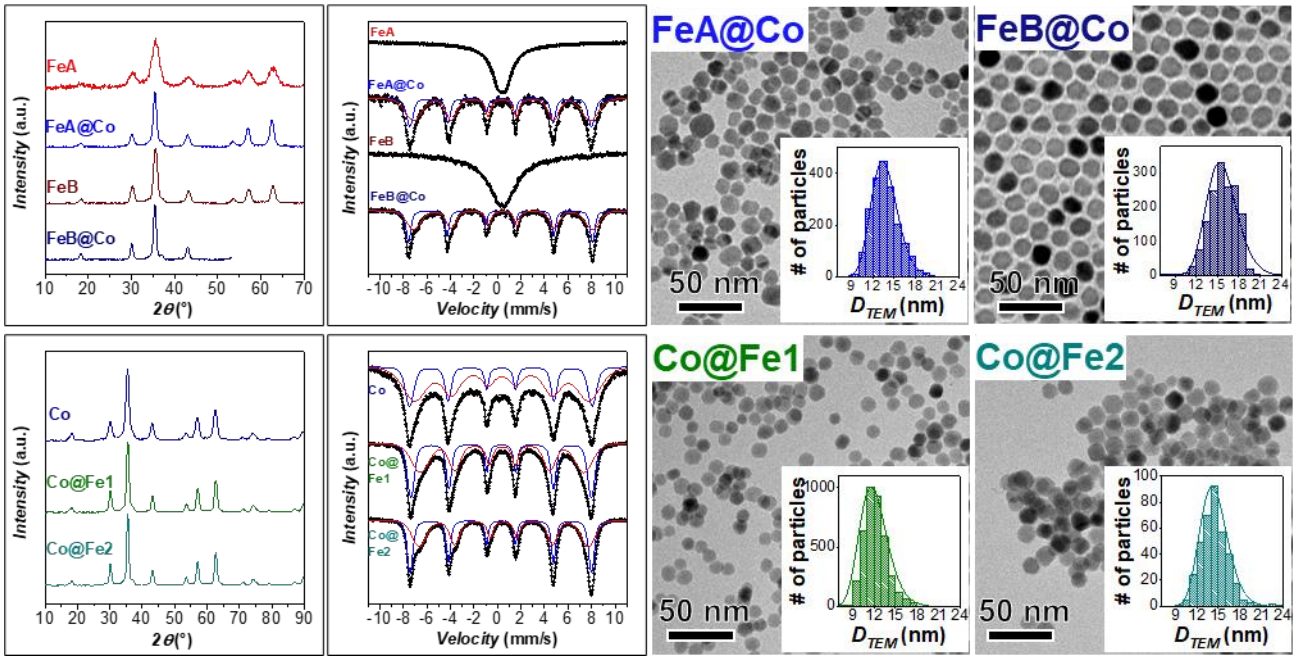

Figure 4. XRD patterns, ^{57}Fe Mössbauer spectra, TEM images, and particle size distribution of the core-shell samples with respective cores

Table 1 reports the cell parameter, crystallite, and particle size of the samples. All core-shell samples feature larger crystallite and particle size than the respective cores, indicating the effective growth of the particles after the second solvothermal treatment. The cell parameters of FeA@Co and FeB@Co are larger than those of the original cores, and in agreement with the presence of cobalt ferrite (a = 8.3919, PDF#022-1086), while Co@Fe1 and Co@Fe2 feature a smaller cell parameter, due to the higher amount of spinel iron oxide (Table 1). The samples were analyzed through RT ^{57}Fe Mössbauer spectroscopy (Figure 4 right, Table 2S**Errore. L'origine riferimento non è stata trovata.**). The iron oxide NPs covered with cobalt ferrite (FeA@Co and FeB@Co) reveal the presence of two sextets in place of the previous singlet present for the respective cores, indicating particles in the blocked state due to the increased particle size and the high magnetocrystalline anisotropy of cobalt ions. The values of the hyperfine fields are larger, as expected, for the larger sample (FeB@Co) if compared to

the smaller one (FeA@Co). The relatively high isomer shift parameters, especially for the octahedral sites (0.39(2) mm/s and 0.46(1) mm/s for FeA@Co and FeB@Co, respectively), indicate the presence of Fe^{II} in the iron oxide cores. Regardless, the values are smaller compared to FeC, having a similar size but entirely composed of iron oxide, therefore having more Fe^{II}. Similar behaviour can be observed for the core-shell samples made up of cobalt ferrite covered with spinel iron oxide (Co@Fe1 and Co@Fe2). The hyperfine field values are lower for the core-shell samples compared with the cobalt ferrite core (labelled Co) because of the presence of the magnetically soft iron oxide, but are higher, due to the larger size, for Co@Fe2 than for Co@Fe1. As for the previous set of samples, the isomer shift values of the octahedral sites are higher when iron oxide-covered cobalt ferrite core, indicating the presence of Fe^{II} and, therefore, not-fully oxidized magnetite.

The core-shell samples were treated by *in-situ* XRD-HTC to study the iron oxide thermal stability in the core or the shell (Figure 5).

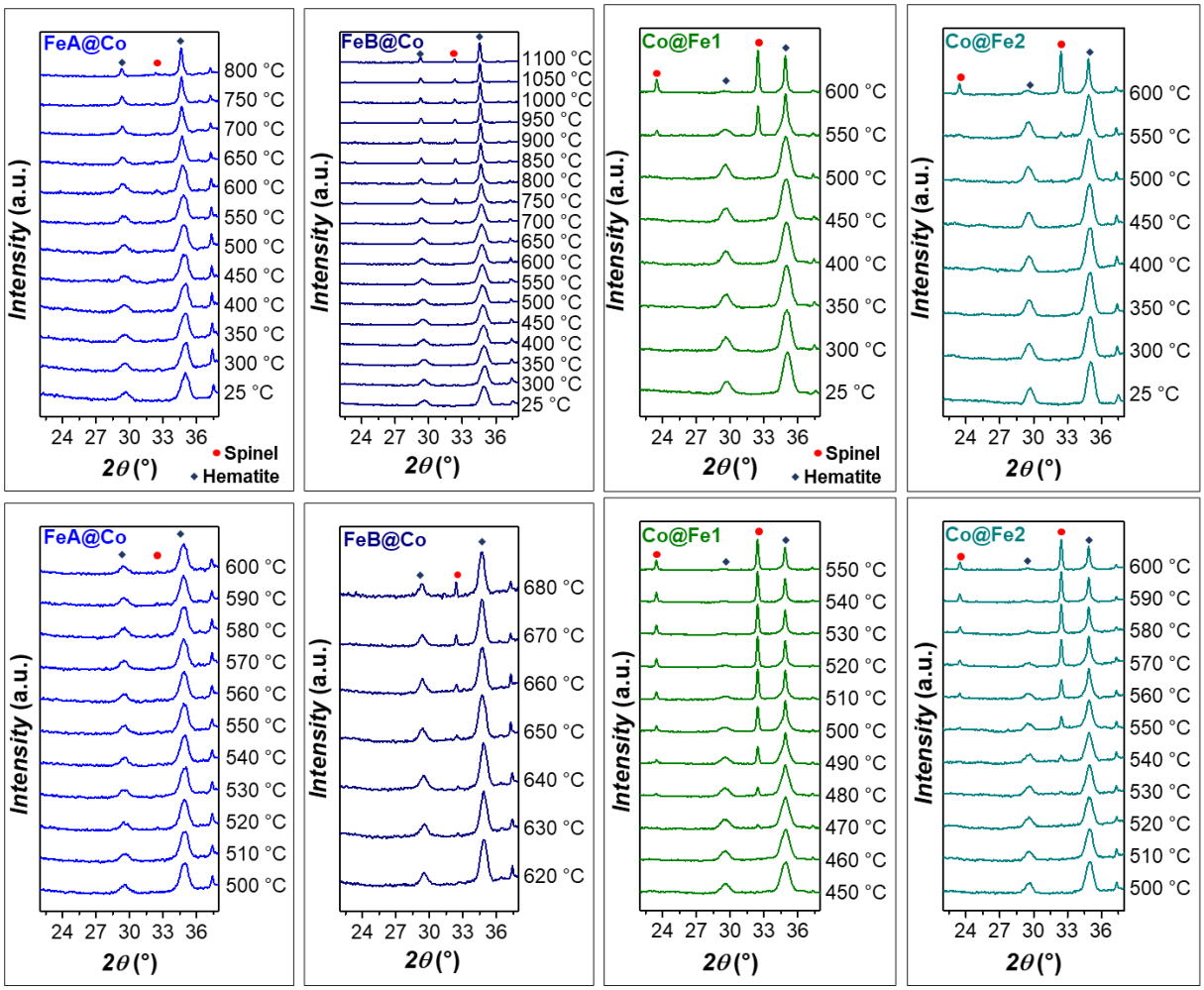

Figure 5. XRD-HTC patterns of the core-shell samples.

FeA@Co was treated from 300 °C to 800 °C with a step of 50 °C, then from 500 °C to 600 °C with a step of 10 °C. It is difficult to catch the hematite peaks at about 24° and 33°, probably due to the cobalt ferrite shell that prevents the maghemite-hematite transition. The Rietveld refinement reveales at the end of the treatment after cooling, 9% w/w of 46 nm hematite and a size increase of the spinel phase from 12.5(1) to 25.9(7) nm (Table 6S). The weight percentage of hematite determined by the Rietveld refinement is consistent with the theoretical fraction of iron oxide in FeA@Co estimated from D_{TEM_V} (6% w/w). In FeB@Co, the hematite peaks are visible thanks to the higher content of iron oxide compared to FeA@Co (23% w/w considering D_{TEM_V}). The Rietveld refinement parameters obtained from the patterns treated in the range 300-1300 °C (Table 7S and Figures 10S1 11S) expose the formation of hematite at 700 °C when the size of the spinel phase is 19.5(4) nm, then

its increase up to 30% w/w at 1000 °C, before going down to 14% w/w, that could be due to solid-state reactions between the phases.[18] After the treatment, at 25°C, the hematite fraction stabilizes at 19%, in agreement with t he theoretical iron oxide content of FeB@Co (23% w/w) indicating, also in this case, that the two phases of iron oxide and cobalt ferrite separated and sintered, as also visible in the TEM micrographs reported in Figure 16S. The size of the spinel phase is stable up to 700 °C when the hematite starts to grow, and it rises to about 100 nm at the end of the thermal treatment. On the contrary, the hematite size is always in the range of 100-90 nm, larger than that of FeA, FeB, and FeC, due to the higher temperatures. The spinel cell parameter constantly increases with the temperature, but when the system cools down, it lowers at a value smaller than the original one (8.384(1) Å *vs*. 8.409(3) Å) due to the absence of Fe^{II}, probably causing lattice contraction. The employment of an inorganic shell permitted to improve the thermal stability of spinel iron oxide, in agreement with previous studies on SnO_2 coated iron oxide NPs,[44] but keeping the ferrimagnetic features of spinel phases.

The samples featuring iron oxide as a shell follow a different behaviour (Figure 5, Tables 8S, 9S, Figures 12S-15S). In Co@Fe1, hematite starts growing at 470 °C and reaches the fraction of 87% w/w at 600 °C, present also at 25 °C after the treatment (theoretical iron oxide content estimated from D_{TEM_V} = 79% w/w). The TEM micrographs of Co@Fe1 treated at 600 °C (Table 8S, Figure 16S) display a micrometric particle featuring indented edges, leading one to imagine that the iron oxide shells sintered together and entrapping the cobalt ferrite nanoparticles. Concerning Co@Fe2, the hematite is visible at 520 °C, and the formation is completed at 600 °C (78 % w/w, Table 9S). The higher temperature found for Co@Fe2 than Co@Fe1 is caused by the thicker shell of Co@Fe2. Considering that the sample FeC presented a lower transition temperature (455 °C) than Co@Fe2 (520°C) and both samples feature similar particle size (about 15 nm), one can think that the cobalt ferrite core preserves the spinel structure against phase transition.

From the comparison between the core-shell samples having similar size (FeA@Co *vs*. Co@Fe1 and FeB@Co *vs*. Co@Fe2) it is clear that when iron oxide is in the core, its thermal stability is increased about one hundred degrees more than when it is in the shell.

2.3 Hydrothermal treatment of spinel iron oxide nanoparticles.

The hydrothermal stability of 10 nm spinel iron oxide nanoparticles (FeB) was tested as a function of water content, temperature, and time, by treating the sample in an autoclave with organic solvents (Table 2).

Table 2. Hydrothermal treatment of the samples. The solvent employed, temperature, time, percentage of hematite (% w/w) calculated by Rietveld refinement, and crystallite size of hematite (H D_{XRD}) and spinel ferrite (M D_{XRD}) phases.

Sample	Toluene (mL)	Pentanol (mL)	Water (mL)	Temperature (°C)	Time (h)	Hematite (%) Rietvled	Hematite (%) Mössbauer	H D_{XRD} (nm)	M D_{XRD} (nm)
FeB	10	10	6	220	10	0	0	-	11.8(2)
FeB_20T_180C_10h	20	0	0	180	10	0	0	-	13.1(2)
FeB_20T0.5W_180C_10h	20	0	0.5	180	10	75(3)	64.4(2)	>100	13.4(7)
FeB_20T1W_180C_10h	20	0	1	180	10	100	100	>100	-
FeB_10T10P1W_200C_5h	10	10	1	200	5	0	0	-	12.3(2)
FeB_10T10P1W_200C_7.5h	10	10	1	200	7.5	0	0	-	11.9(3)
FeB_10T10P1W_200C_10h	10	10	1	200	10	15(1)	12(1)	74(8)	13.3(2)
FeB_10T10P1W_220C_5h	10	10	1	220	5	2.9(4)	1.6(5)	>100	13.1(2)
FeB_10T10P1W_220C_7.5h	10	10	1	220	7.5	7(3)	3.0(1)	>100	14.7(2)
FeB_10T10P1W_220C_10h	10	10	1	220	10	12.8(5)	9.9(2)	77(6)	19.8(2)
FeB_10T10P2W_220C_10h	10	10	2	220	10	82(3)	73.7(2)	>100	20.7(2)
FeB_10T10P5W_220C_10h	10	10	5	220	10	100	100	>100	-
Co@Fe1	10	10	5	220	10	0	0	-	14.3(1)
Co@Fe1_10T10P1W_220C_10h	10	10	1	220	10	2.7(6)	5.3(1)	>100	18.9(2)

Firstly, FeB was treated with toluene at 180 °C for 10 hours without additional water. The crystallite size of spinel iron oxide increased from 11.8(1) nm to 13.1(2) nm. The ^{57}Fe Mössbauer spectrum of the sample shows a broad singlet caused by the NPs in the edge between the superparamagnetic and

the blocked state (Figure 6). Secondly, the sample FeB was treated with toluene at 180 °C for 10 hours, with 0.5 or 1 mL of water. In both the treatments, hematite is formed, as evidenced from XRD patterns and ^{57}Fe Mössbauer spectra (Figure 6, Figure 17S), but in the first case, a small fraction of spinel iron oxide is still present (25% w/w).

Instead of pure toluene as solvent, toluene : pentanol mixture (1:1) was employed together with 1 mL of water at 200 °C, for 5, 7.5, and 10 hours to control the hematite formation better. At 5 and 7.5 hours, hematite did not form, and the crystallite size of spinel iron oxide was kept at about 12 nm (Table 2). However, in the ^{57}Fe Mössbauer spectra, some differences are visible compared to FeB. Indeed, two sextets of different broadness arise with an additional broad singlet in the 5h-200°C-sample. The presence of sextets, indicating magnetically blocked NPs, may be caused by the presence of magnetite, which has higher magnetocrystalline anisotropy than maghemite ($1.3 \cdot 10^4$ Jm^{-3} *vs.* $5 \cdot 10^3$ Jm^{-3}). Only after 10 hours, 15% of micrometric hematite is formed, confirming the time-dependence of spinel iron oxide-hematite transition, as seen above for the *in-situ* XRD analyses.

This dependence could also be evidenced when the temperature is raised to 220 °C. Indeed, after 5, 7.5, and 10 hours, the hematite content increased from 2.9% to 7% and 12.8%, respectively. The size of the spinel phase in these samples was found to be 13.1 nm, 14.7 nm, and 19.8 nm, respectively. The growth of the particles (also in the 5h-220°C-sample) is coherent with their Mössbauer spectra. Indeed, all spectra were best ascribed with two sextets corresponding to the interstitial sites of the spinel structure with an additional sextet from the hematite structure. For the 10h-220°C sample, the TEM micrograph reported in Figure 18S shows spheroidal NPs with sizes ranging from 15 to 30 nm, compatible with the crystallite sizes and high dispersity. Based on the shape and size of the particles, we can hypothesize that the larger and faceted ones are composed of hematite, while the smaller and spheroidal ones belong to spinel iron oxide.

Finally, changes in the water content were tested at 220 °C for 10 hours. The hematite fraction resulted in about 13%, 80%, and 100% for 1, 2, and 5 mL of water, respectively, indicating that the spinel iron oxide-hematite transition strongly depends on the water amount.

The spinel iron oxide hydrothermal stability was also investigated as the shell in the sample Co@Fe1, by treating the sample at 220 °C for 10 hours with 10 mL of toluene, 10 mL of pentanol, and 1 mL of water. The hematite content was estimated to be about 2.7% w/w, while the crystallite size of the spinel phase increased from 14.3 nm to 18.9 nm, reaching a final size similar to the sample FeB treated under the same experimental condition. The ^{57}Fe Mössbauer spectrum shows the sextet ascribable to hematite, and the two sextets of the O_h and T_d sites of the spinel structure. Compared with the hyperfine parameters of the spinel phase of the original Co@Fe1 (Table 10S), the treated sample features a higher hyperfine field (due to the larger size) and isomer shift, indicating a higher abundance of Fe^{II} in the spinel structure. Once again, as evidenced in the TEM micrographs of Figure 18S, larger faceted particles are present, but in a lower amount if compared to the treated FeB, confirming the role of the cobalt ferrite core in preserving the spinel structure against phase transition.

In all the above experiments, several aspects can be summarized. The water content causes the hematite formation, reaching the complete transition with 5 mL. Moreover, as observed in the *in-situ* XRD analyses, the transition was found to be time- and, to a lower extent, temperature-sensitive. Better control over the phase transition was obtained by replacing toluene with pentanol, probably due to the higher reducing potential of this latter solvent.[59,60] This behaviour can be better appreciated in the tests performed at 220°C, where the isomer shift of the sextets in the Mössbauer spectra (Table 10S) show values close to the bulk magnetite (0.67 mm/s),[61,62] that increase with time, due to the longer contact between pentanol and iron oxide. This effect is also visible for the core-shell sample Co@Fe1, where O_h sites have an isomer shift of 0.61 mm/s indicating the presence of magnetite in the shell. Indeed, only 3% w/w of hematite formed, well below the theoretical iron oxide content of about 80% w/w (Table 1). This result indicates the combined effect of the cobalt

ferrite core, which stabilizes the spinel iron oxide structure, and the pentanol reducing behaviour, preventing the formation of maghemite and its transition into hematite. Further, the accuracy of Mössbauer spectroscopy deserves attention, particularly concerning the detection of hematite. Indeed, the generated hematite phase features, for all samples, similar hyperfine parameters (δ = 0.376(9) mm/s; B_{HF} = 51.6(1) T; Qs = -0.22(2) mm/s; FWHM = 0.22(6), Table 10S), and the fraction calculated from the relative spectra intensity matches the Rietveld fraction with a better agreement when the hematite content is above 10% w/w.

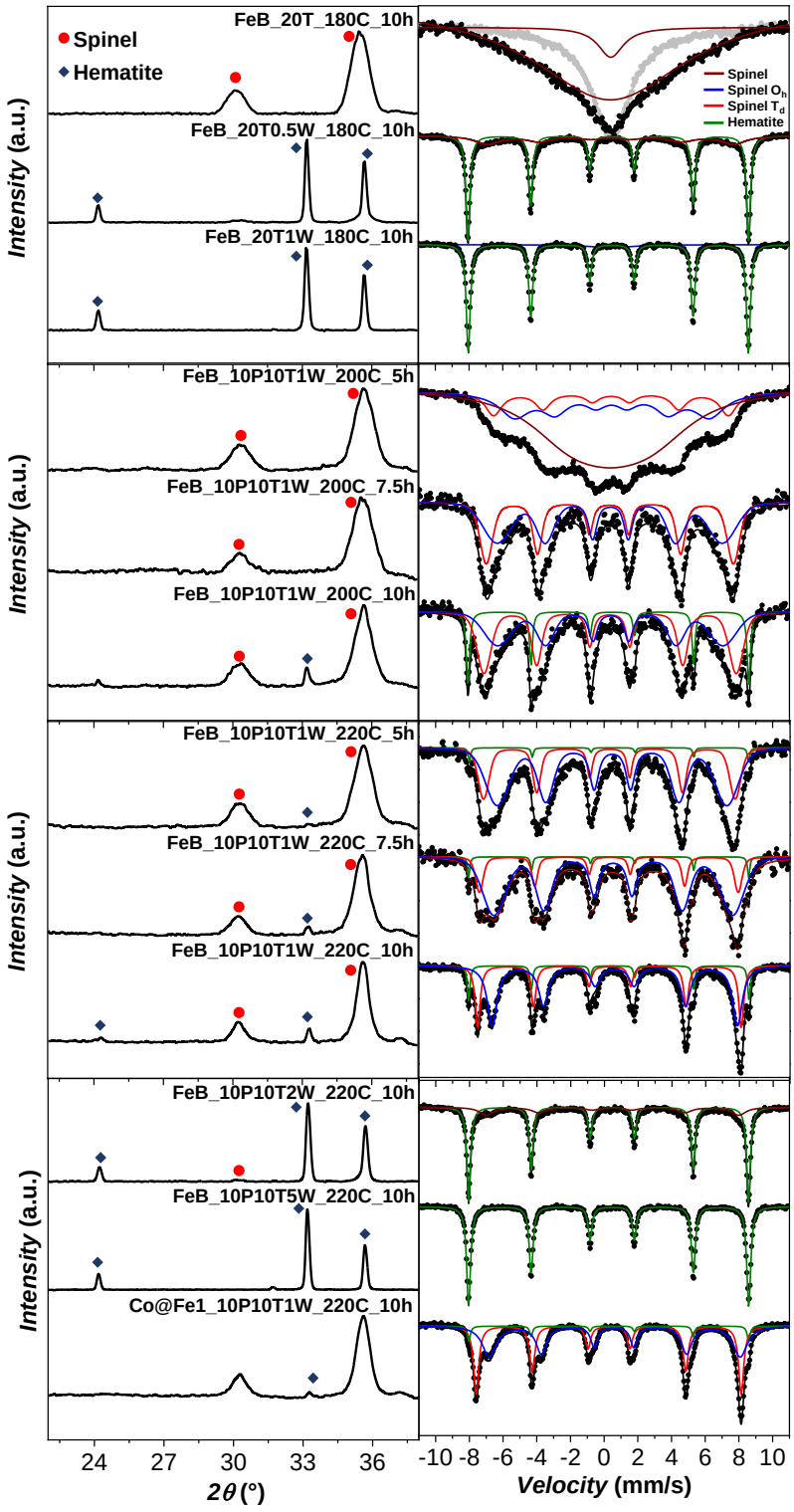

Figure 6. XRD patterns (left) and corresponding RT ^{57}Fe Mössbauer spectra (right) of the FeB and Co@Fe1 after hydrothermal treatments under the different conditions reported in **Table 2**. In grey the untreated FeB sample.

3. CONCLUSION

Thermal and hydrothermal stability of nanosized spinel iron oxide was studied as single-particle, core, and shell in heterostructures. The spinel iron oxide-hematite transition was found to be 360 °C for the 6 nm sample, the temperature at which the oleate molecules decomposes, favouring the contact among the particles and the sintering. The larger 10 and 15 nm NPs displayed instead of a transition temperature at about 455 °C. For the core-shell nano-heterostructures, the transition temperature increases to 470 and 520 °C when iron oxide is in the shell, and about 630 °C when it is in the core, while cobalt ferrite remains stable up to 1000 °C, indicating a stabilizing effect of cobalt ferrite toward the phase transition. By treating the 10 nm spinel iron oxide sample in an autoclave, it was found that the transition depends mainly on water amount, and to a lower extent on time and temperature, transforming nanometric spinel iron oxide into micrometric hematite crystals. The transition is complete when 5 mL of water is employed in the synthesis. The ^{57}Fe Mössbauer spectroscopy revealed an increase of Fe^{II} in the octahedral sites of the spinel structure, indicating a reducing effect of pentanol. The cobalt ferrite core-iron oxide shell, treated in the autoclave, revealed the obtainment of about only 3% w/w of micrometric hematite, despite the 80% w/w of theoretical iron oxide shell. Furthermore, the presence of isomer shift with values close to the bulk magnetite indicates the formation of magnetite-coated cobalt ferrite NPs. This result was achieved due to the stabilizing effect of the cobalt ferrite core toward the spinel structure and the reducing behaviour of pentanol, avoiding the magnetite→maghemite→hematite transition. In all the cases, the hematite content estimated by Rietveld's refinement of the XRD pattern was comparable with the one from ^{57}Fe Mössbauer spectra. Finally, besides providing direct information on the spinel iron oxide stability and crystalline phase evolution, the thermal and hydrothermal treatments suggest possible synthetic strategies for the

development of heterostructured or composite materials, with tunable magnetic properties, from hard-soft ferrimagnetism to antiferromagnetism.

ACKNOWLEDGMENTS

“PON AIM (PON Ricerca e Innovazione 2014 – 2020-Azione I.2-D.D. n.407 del 27 Febbraio 2018 "Attraction and International Mobility", Cult-GeoChim project n. AIM1890410-3)" and CESA Project - RAS Piano Sulcis" (CUP: E58C16000080003) are gratefully acknowledged for financing the fixed-term researcher fellowship of V. Mameli and the post-doctoral fellowship of M. Sanna Angotzi. Thanks are due to Dr Andrea Ardu and to the "Centro Servizi di Ateneo per la Ricerca (CeSAR)" for the use of the TEM measurements performed with JEOL JEM 1400 PLUS and JEOL JEM 2010 URP equipped with Gatan Image Filter. Prof. Stefano Enzo is gratefully acknowledged for the fruitful discussion on XRD data. This work was supported by the "Fondazione di Sardegna, Italy, Fondazione di Sardegna (FdS)" Project: CUP F72F20000240007(2019): "Surface-tailored Materials for Sustainable Environmental Applications". This work has been supported by Charles University Research Centre program No. UNCE/SCI/014.

ELECTRONIC SUPPLEMENTARY MATERIAL

Supplementary material (Synthesis parameters, Mössbauer data, Thermogravimetric analyses, Rietveld refinements, Additional TEM micrographs, Data on hydrothermal treatments) is available in the online version of this article at http://dx.doi.org/10.1007/**********.

[1] A.G. Roca, L. Gutiérrez, H. Gavilán, M.E. Fortes Brollo, S. Veintemillas-Verdaguer, M. del P. Morales, Design strategies for shape-controlled magnetic iron oxide nanoparticles, Adv. Drug Deliv. Rev. 138 (2019) 68–104. https://doi.org/10.1016/j.addr.2018.12.008.

[2] C. Song, W. Sun, Y. Xiao, X. Shi, Ultrasmall iron oxide nanoparticles: synthesis, surface modification, assembly, and biomedical applications, Drug Discov. Today. 24 (2019) 835–

844. https://doi.org/10.1016/j.drudis.2019.01.001.

[3] R.M. Cornell, U. Schwertmann, The Iron Oxides, Wiley, 2003. https://doi.org/10.1002/3527602097.

[4] E.A. Campos, D.V.B. Stockler Pinto, J.I.S. de Oliveira, E. da C. Mattos, R. de C.L. Dutra, Synthesis, Characterization and Applications of Iron Oxide Nanoparticles - a Short Review, J. Aerosp. Technol. Manag. 7 (2015) 267–276. https://doi.org/10.5028/jatm.v7i3.471.

[5] S. Shylesh, V. Schünemann, W.R. Thiel, Magnetically separable nanocatalysts: Bridges between homogeneous and heterogeneous catalysis, Angew. Chemie - Int. Ed. 49 (2010) 3428–3459. https://doi.org/10.1002/anie.200905684.

[6] J. Dulińska-Litewka, A. Łazarczyk, P. Hałubiec, O. Szafrański, K. Karnas, A. Karewicz, Superparamagnetic iron oxide nanoparticles-current and prospective medical applications, Materials (Basel). 12 (2019). https://doi.org/10.3390/ma12040617.

[7] S.M. Dadfar, K. Roemhild, N.I. Drude, S. von Stillfried, R. Knüchel, F. Kiessling, T. Lammers, Iron oxide nanoparticles: Diagnostic, therapeutic and theranostic applications, Adv. Drug Deliv. Rev. 138 (2019) 302–325. https://doi.org/10.1016/j.addr.2019.01.005.

[8] R. Bhateria, R. Singh, A review on nanotechnological application of magnetic iron oxides for heavy metal removal, J. Water Process Eng. 31 (2019) 100845. https://doi.org/10.1016/j.jwpe.2019.100845.

[9] M. Usman, J.M. Byrne, A. Chaudhary, S. Orsetti, K. Hanna, C. Ruby, A. Kappler, S.B. Haderlein, Magnetite and Green Rust: Synthesis, Properties, and Environmental Applications of Mixed-Valent Iron Minerals, Chem. Rev. 118 (2018) 3251–3304. https://doi.org/10.1021/acs.chemrev.7b00224.

[10] P. Xu, G.M. Zeng, D.L. Huang, C.L. Feng, S. Hu, M.H. Zhao, C. Lai, Z. Wei, C. Huang, G.X. Xie, Z.F. Liu, Use of iron oxide nanomaterials in wastewater treatment: A review, Sci. Total Environ. 424 (2012) 1–10. https://doi.org/10.1016/j.scitotenv.2012.02.023.

[11] S.I. Siddiqui, S.A. Chaudhry, Iron oxide and its modified forms as an adsorbent for arsenic removal: A comprehensive recent advancement, Process Saf. Environ. Prot. 111 (2017) 592–626. https://doi.org/10.1016/j.psep.2017.08.009.

[12] J.M.D. Coey, Magnetism and magnetic materials, Cambridge University Press, Cambridge, 2009. https://doi.org/10.1016/0160-9327(88)90178-0.

[13] M. Sanna Angotzi, V. Mameli, S. Khanal, M. Veverka, J. Vejpravova, C. Cannas, Effect of different molecular coatings on the heating properties of maghemite nanoparticles, Nanoscale Adv. 4 (2022) 408–420. https://doi.org/10.1039/D1NA00478F.

[14] S. Khanal, M. Sanna Angotzi, V. Mameli, M. Veverka, H.L. Xin, C. Cannas, J. Vejpravová, Self-Limitations of Heat Release in Coupled Core-Shell Spinel Ferrite Nanoparticles: Frequency, Time, and Temperature Dependencies, Nanomaterials. 11 (2021) 2848. https://doi.org/10.3390/nano11112848.

[15] M. Sanna Angotzi, V. Mameli, C. Cara, K.B.L. Borchert, C. Steinbach, R. Boldt, D. Schwarz, C. Cannas, Meso- and macroporous silica-based arsenic adsorbents: effect of pore size, nature of the active phase, and silicon release, Nanoscale Adv. 3 (2021) 6100–6113. https://doi.org/10.1039/D1NA00487E.

[16] M. Sanna Angotzi, V. Mameli, C. Cara, A. Musinu, C. Sangregorio, D. Niznansky, H.L. Xin, J. Vejpravova, C. Cannas, Coupled hard–soft spinel ferrite-based core–shell nanoarchitectures: magnetic properties and heating abilities, Nanoscale Adv. 2 (2020) 3191–3201. https://doi.org/10.1039/D0NA00134A.

[17] C. Cara, E. Rombi, A. Musinu, V. Mameli, A. Ardu, M. Sanna Angotzi, L. Atzori, D. Niznansky, H.L. Xin, C. Cannas, MCM-41 support for ultrasmall γ-Fe 2 O 3 nanoparticles for H 2 S removal, J. Mater. Chem. A. 5 (2017) 21688–21698. https://doi.org/10.1039/C7TA03652C.

[18] I. V Chernyshova, M.F. Hochella Jr, A.S. Madden, Size-dependent structural transformations of hematite nanoparticles. 1. Phase transition, Phys. Chem. Chem. Phys. 9 (2007) 1736. https://doi.org/10.1039/b618790k.

[19] K. Liang, L.S. Hui, A. Turak, Probing the multi-step crystallization dynamics of micelle templated nanoparticles: Structural evolution of single crystalline γ-Fe 2 O 3, Nanoscale. 11 (2019) 9076–9084. https://doi.org/10.1039/c9nr00148d.

[20] G. Schimanke, In situ XRD study of the phase transition of nanocrystalline maghemite (γ-Fe2O3) to hematite (α-Fe2O3), Solid State Ionics. 136–137 (2000) 1235–1240. https://doi.org/10.1016/S0167-2738(00)00593-2.

[21] H. Guo, A.S. Barnard, Thermodynamics of Iron Oxides and Oxyhydroxides in Different Environments, Iron Oxides From Nat. to Appl. (2016) 269–292. https://doi.org/10.1002/9783527691395.ch12.

[22] P. Ayyub, M. Multani, M. Barma, V.R. Palkar, R. Vijayaraghavan, Size-induced structural phase transitions and hyperfine properties of microcrystalline Fe2O3, J. Phys. C Solid State Phys. 21 (1988) 2229–2245. https://doi.org/10.1088/0022-3719/21/11/014.

[23] A. Navrotsky, L. Mazeina, J. Majzlan, Size-driven structural and thermodynamic complexity in iron oxides, Science (80-.). 319 (2008) 1635–1638. https://doi.org/10.1126/science.1148614.

[24] Y. El Mendili, J.F. Bardeau, N. Randrianantoandro, F. Grasset, J.M. Greneche, Insights into

the mechanism related to the phase transition from γ-Fe 2O 3 to α-Fe 2O 3 nanoparticles induced by thermal treatment and laser irradiation, J. Phys. Chem. C. 116 (2012) 23785–23792. https://doi.org/10.1021/jp308418x.

[25] L. Machala, J. Tuček, R. Zbořil, Polymorphous Transformations of Nanometric Iron(III) Oxide: A Review, Chem. Mater. 23 (2011) 3255–3272. https://doi.org/10.1021/cm200397g.

[26] Y.H. Chen, Thermal properties of nanocrystalline goethite, magnetite, and maghemite, J. Alloys Compd. 553 (2013) 194–198. https://doi.org/10.1016/j.jallcom.2012.11.102.

[27] A. Sathya, T.R. Ravindran, J. Philip, Superior thermal stability of polymer capped Fe3O4 magnetic nanoclusters, J. Am. Ceram. Soc. 101 (2018) 483–491. https://doi.org/10.1111/jace.15197.

[28] T. Ninjbadgar, S. Yamamoto, M. Takano, Thermal properties of the γ-Fe2O3/poly(methyl methacrylate) core/shell nanoparticles, Solid State Sci. 7 (2005) 33–36. https://doi.org/10.1016/j.solidstatesciences.2004.10.030.

[29] F.S. Yen, W.C. Chen, J.M. Yang, C.T. Hong, Crystallite Size Variations of Nanosized Fe2O3 Powders during γ- To α-Phase Transformation, Nano Lett. 2 (2002) 245–252. https://doi.org/10.1021/nl010089m.

[30] A. Radoń, M. Kądziołka-Gaweł, D. Łukowiec, P. Gębara, K. Cesarz-Andraczke, A. Kolano-Burian, P. Włodarczyk, M. Polak, R. Babilas, Influence of magnetite nanoparticles shape and spontaneous surface oxidation on the electron transport mechanism, Materials (Basel). 14 (2021). https://doi.org/10.3390/ma14185241.

[31] M.A. Vacca, C. Cara, V. Mameli, M. Sanna Angotzi, M.A. Scorciapino, M.G. Cutrufello, A. Musinu, V. Tyrpekl, L. Pala, C. Cannas, Hexafluorosilicic Acid (FSA): from Hazardous Waste to Precious Resource in Obtaining High Value-Added Mesostructured Silica, ACS

Sustain. Chem. Eng. 8 (2020) 14286–14300. https://doi.org/10.1021/acssuschemeng.0c03218.

[32] C. Cara, V. Mameli, E. Rombi, N. Pinna, M. Sanna Angotzi, D. Nižňanský, A. Musinu, C. Cannas, Anchoring ultrasmall FeIII-based nanoparticles on silica and titania mesostructures for syngas H2S purification, Microporous Mesoporous Mater. 298 (2020) 110062. https://doi.org/10.1016/j.micromeso.2020.110062.

[33] C. Cara, E. Rombi, A. Ardu, M.A. Vacca, C. Cannas, Sub-Micrometric MCM-41 Particles as Support to Design Efficient and Regenerable Maghemite-Based Sorbent for H 2 S Removal, J. Nanosci. Nanotechnol. 19 (2019) 5035–5042. https://doi.org/10.1166/jnn.2019.16800.

[34] C. Cara, E. Rombi, V. Mameli, A. Ardu, M. Sanna Angotzi, D. Niznansky, A. Musinu, C. Cannas, γ-Fe 2 O 3 -M41S Sorbents for H 2 S Removal: Effect of Different Porous Structures and Silica Wall Thickness, J. Phys. Chem. C. 122 (2018) 12231–12242. https://doi.org/10.1021/acs.jpcc.8b01487.

[35] L.Q. Yu, Y.H. Wen, M. Yan, Exchange bias of MnFe2O4@γFe2O3 and CoFe2O4@γFe2O3 core/shell nanoparticles, 283 (2004) 353–356. http://ac.els-cdn.com/S0304885304006559/1-s2.0-S0304885304006559-main.pdf?_tid=2f377ef4-7c79-11e3-9e0a-00000aab0f01&acdnat=1389634748_360589ee663e5272d805b3058c459666.

[36] J. a. Gomes, G.M. Azevedo, J. Depeyrot, J. Mestnik-Filho, F.L.O. Paula, F. a. Tourinho, R. Perzynski, Structural, Chemical, and Magnetic Investigations of Core–Shell Zinc Ferrite Nanoparticles, J. Phys. Chem. C. 116 (2012) 24281–24291. https://doi.org/10.1021/jp3055069.

[37] R. Frison, G. Cernuto, A. Cervellino, O. Zaharko, G.M. Colonna, A. Guagliardi, N. Masciocchi, Magnetite-maghemite nanoparticles in the 5-15 nm range: Correlating the core-

shell composition and the surface structure to the magnetic properties. A total scattering study., Chem. Mater. 25 (2013) 4820–4827. https://doi.org/10.1021/cm403360f.

[38] J.-H. Lee, J.-T. Jang, J.-S. Choi, S.H. Moon, S.-H. Noh, J.-G.J.-W.J.-G.J.-W. Kim, J.-G.J.-W.J.-G.J.-W. Kim, I.-S. Kim, K.I. Park, J. Cheon, Exchange-coupled magnetic nanoparticles for efficient heat induction., Nat. Nanotechnol. 6 (2011) 418–422. https://doi.org/10.1038/nnano.2011.95.

[39] S. Liébana-Viñas, K. Simeonidis, U. Wiedwald, Z.-A. Li, Z. Ma, E. Myrovali, A. Makridis, D. Sakellari, G. Vourlias, M. Spasova, M. Farle, M. Angelakeris, Optimum nanoscale design in ferrite based nanoparticles for magnetic particle hyperthermia, RSC Adv. 6 (2016) 72918–72925. https://doi.org/10.1039/C6RA17892H.

[40] J. Robles, R. Das, M. Glassell, M.H. Phan, H. Srikanth, Exchange-coupled Fe3O4/CoFe2O4 nanoparticles for advanced magnetic hyperthermia, AIP Adv. 8 (2018) 2–8. https://doi.org/10.1063/1.5007249.

[41] A. Sathya, P. Guardia, R. Brescia, N. Silvestri, G. Pugliese, S. Nitti, L. Manna, T. Pellegrino, CoxFe3-xO4Nanocubes for Theranostic Applications: Effect of Cobalt Content and Particle Size, Chem. Mater. 28 (2016) 1769–1780. https://doi.org/10.1021/acs.chemmater.5b04780.

[42] M. Sanna Angotzi, V. Mameli, C. Cara, D. Peddis, H.L. Xin, C. Sangregorio, M.L. Mercuri, C. Cannas, On the synthesis of bi-magnetic manganese ferrite-based core–shell nanoparticles, Nanoscale Adv. 3 (2021) 1612–1623. https://doi.org/10.1039/D0NA00967A.

[43] M. Sanna Angotzi, A. Musinu, V. Mameli, A. Ardu, C. Cara, D. Niznansky, H.L. Xin, C. Cannas, Spinel Ferrite Core–Shell Nanostructures by a Versatile Solvothermal Seed-Mediated Growth Approach and Study of Their Nanointerfaces, ACS Nano. 11 (2017) 7889–7900. https://doi.org/10.1021/acsnano.7b02349.

[44] X. Xu, M. Ge, C. Wang, J.Z. Jiang, High temperature stable monodisperse superparamagnetic core-shell iron-oxide@SnO2 nanoparticles, Appl. Phys. Lett. 95 (2009) 183112. https://doi.org/10.1063/1.3261756.

[45] M. Sanna Angotzi, V. Mameli, C. Cara, A. Musinu, C. Sangregorio, D. Niznansky, H.L. Xin, J. Vejpravova, C. Cannas, Coupled hard-soft spinel ferrite-based core-shell nanoarchitectures: Magnetic properties and heating abilities, Nanoscale Adv. 2 (2020) 3191–3201. https://doi.org/10.1039/d0na00134a.

[46] A. López-Ortega, M. Estrader, G. Salazar-Alvarez, A.G. Roca, J. Nogués, Applications of exchange coupled bi-magnetic hard/soft and soft/hard magnetic core/shell nanoparticles, Phys. Rep. 553 (2015) 1–32. https://doi.org/10.1016/j.physrep.2014.09.007.

[47] M. Fantauzzi, F. Secci, M. Sanna Angotzi, C. Passiu, C. Cannas, A. Rossi, Nanostructured spinel cobalt ferrites: Fe and Co chemical state, cation distribution and size effects by X-ray photoelectron spectroscopy, RSC Adv. 9 (2019) 19171–19179. https://doi.org/10.1039/C9RA03488A.

[48] M. Sanna Angotzi, V. Mameli, C. Cara, A. Ardu, D. Nizňnanský, A. Musinu, Oleate-Based Solvothermal Approach for Size Control of M II Fe 2 III O 4 (M II ═ Mn II , Fe II) Colloidal Nanoparticles, J. Nanosci. Nanotechnol. 19 (2019) 4954–4963. https://doi.org/10.1166/jnn.2019.16785.

[49] V. Mameli, M. Sanna Angotzi, C. Cara, C. Cannas, Liquid Phase Synthesis of Nanostructured Spinel Ferrites—A Review, J. Nanosci. Nanotechnol. 19 (2019) 4857–4887. https://doi.org/10.1166/jnn.2019.16808.

[50] M. Sanna Angotzi, V. Mameli, A. Musinu, D. Nizňnanský, 57 Fe Mössbauer Spectroscopy for the Study of Nanostructured Mixed Mn–Co Spinel Ferrites, J. Nanosci. Nanotechnol. 19

(2019) 5008–5013. https://doi.org/10.1166/jnn.2019.16793.

[51] M. Sanna Angotzi, V. Mameli, D. Zákutná, D. Kubániová, C. Cara, C. Cannas, Evolution of the Magnetic and Structural Properties with the Chemical Composition in Oleate-Capped Mn x Co 1– x Fe 2 O 4 Nanoparticles, J. Phys. Chem. C. 125 (2021) 20626–20638. https://doi.org/10.1021/acs.jpcc.1c06211.

[52] M. Sanna Angotzi, V. Mameli, C. Cara, V. Grillo, S. Enzo, A. Musinu, C. Cannas, Defect-assisted synthesis of magneto-plasmonic silver-spinel ferrite heterostructures in a flower-like architecture, Sci. Rep. 10 (2020) 17015. https://doi.org/10.1038/s41598-020-73502-5.

[53] T.A.S. Ferreira, J.C. Waerenborgh, M.H.R.M. Mendonça, M.R. Nunes, F.M. Costa, Structural and morphological characterization of FeCo2O4and CoFe2O4spinels prepared by a coprecipitation method, Solid State Sci. 5 (2003) 383–392. https://doi.org/10.1016/S1293-2558(03)00011-6.

[54] L. Lutterotti, P. Scardi, Simultaneous structure and size–strain refinement by the Rietveld method, J. Appl. Crystallogr. 23 (1990) 246–252. https://doi.org/10.1107/S0021889890002382.

[55] R.A. Young, D.B. Wiles, Profile shape functions in Rietveld refinements, J. Appl. Crystallogr. 15 (1982) 430–438. https://doi.org/10.1107/S002188988201231X.

[56] S. Mondini, A.M. Ferretti, A. Puglisi, A. Ponti, Pebbles and PebbleJuggler: software for accurate, unbiased, and fast measurement and analysis of nanoparticle morphology from transmission electron microscopy (TEM) micrographs, Nanoscale. 4 (2012) 5356. https://doi.org/10.1039/c2nr31276j.

[57] X. Ye, D. Lin, Z. Jiao, L. Zhang, The thermal stability of nanocrystalline maghemite Fe2O3, J. Phys. D. Appl. Phys. 31 (1998) 2739–2744. https://doi.org/10.1088/0022-3727/31/20/006.

[58] T. Belin, N. Millot, N. Bovet, M. Gailhanou, In situ and time resolved study of the - transition in nanometric particles, J. Solid State Chem. 180 (2007) 2377–2385. https://doi.org/10.1016/j.jssc.2007.06.013.

[59] J.R. Bernardo, A.C. Fernandes, Deoxygenation of carbonyl compounds using an alcohol as an efficient reducing agent catalyzed by oxo-rhenium complexes, Green Chem. 18 (2016) 2675–2681. https://doi.org/10.1039/c5gc02777b.

[60] C. D'Agostino, S. Chansai, I. Bush, C. Gao, M.D. Mantle, C. Hardacre, S.L. James, L.F. Gladden, Assessing the effect of reducing agents on the selective catalytic reduction of NOx over Ag/Al2O3 catalysts, Catal. Sci. Technol. 6 (2016) 1661–1666. https://doi.org/10.1039/c5cy01508a.

[61] B. Fultz, Mössbauer Spectrometry, Charact. Mater. (2011). https://doi.org/10.1002/0471266965.

[62] E. Murad, J.H. Johnston, Iron Oxides and Oxyhydroxides, Mössbauer Spectrosc. Appl. to Inorg. Chem. (1987) 507–583.